

Viscoplasticity using peridynamics

J. T. Foster^{1,*}, S. A. Silling¹ and W. W. Chen²

¹*Sandia National Laboratories, 1515 Eubank Blvd. SE, Albuquerque, NM 87123, U.S.A.*

²*Purdue University, 3323 Neil Armstrong Hall of Engineering, 701 W. Stadium Ave., West Lafayette, IN 47907, U.S.A.*

SUMMARY

Peridynamics is a continuum reformulation of the standard theory of solid mechanics. Unlike the partial differential equations of the standard theory, the basic equations of peridynamics are applicable even when cracks and other singularities appear in the deformation field. The assumptions in the original peridynamic theory resulted in severe restrictions on the types of material response that could be modeled, including a limitation on the Poisson ratio. Recent theoretical developments have shown promise for overcoming these limitations, but have not previously incorporated rate dependence and have not been demonstrated in realistic applications. In this paper, a new method for implementing a rate-dependent plastic material within a peridynamic numerical model is proposed and demonstrated. The resulting material model implementation is fitted to rate-dependent test data on 6061-T6 aluminum alloy. It is shown that with this material model, the peridynamic method accurately reproduces the experimental results for Taylor impact tests over a wide range of impact velocities. The resulting model retains the advantages of the peridynamic formulation regarding discontinuities while allowing greater generality in material response than was previously possible. Copyright © 2009 John Wiley & Sons, Ltd.

Received 13 November 2008; Revised 4 May 2009; Accepted 10 July 2009

KEY WORDS: peridynamics; peridynamic states; plasticity; non-local theory; integral equations; continuum mechanics; Taylor impact

1. INTRODUCTION

The peridynamic model [1–3] is a continuum reformulation of the classical partial differential equation of motion (conservation of momentum). It has been most notably used to model the deformation of bodies in which discontinuities (i.e. cracks) occur spontaneously. The basic equations are applicable even when singularities appear in the deformation field. These discontinuous deformations would lead to an inability to evaluate spatial derivatives in the classical formulation and

*Correspondence to: J. T. Foster, PO Box 5800, MS 1160, Albuquerque, NM 87185, U.S.A.

†E-mail: jtfoste@sandia.gov

Contract/grant sponsor: DOE/DoD Joint Munitions Technology Program

Copyright © 2009 John Wiley & Sons, Ltd.

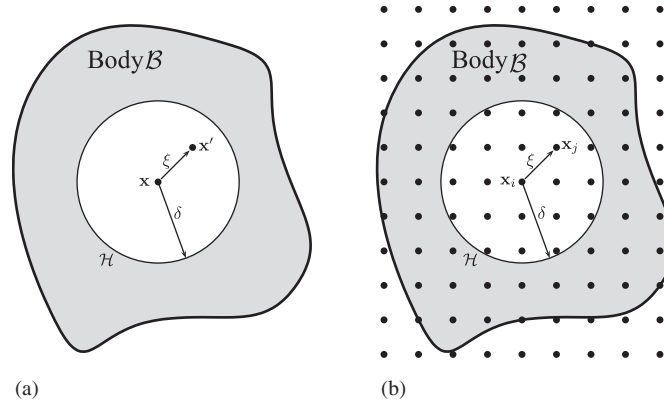


Figure 1. Schematic of peridynamic representations: (a) continuum and (b) discrete.

special techniques would be required to analyze the problem. Recalling from classical continuum theory the conservation of momentum equation shown as follows[‡]:

$$\rho \ddot{\mathbf{u}}[\mathbf{x}, t] = \nabla \cdot \boldsymbol{\sigma}[\mathbf{x}, t] + \mathbf{b}[\mathbf{x}, t] \quad (1)$$

where ρ , \mathbf{u} , \mathbf{b} are statistically defined quantities representing continuum notions of mass density, vector-valued displacement, and body force density, respectively. $\boldsymbol{\sigma}$ is a symmetric second-order tensor that satisfies the equation, typically called the first Piola–Kirchhoff stress tensor. The dependent variables \mathbf{x} and t are defined as a position vector in the reference configuration and time, respectively.

In the peridynamic model, the second term on the right-hand side of Equation (1), called the divergence of the stress tensor, is replaced with an integral functional. The functional relates pairwise forces or ‘bonds’ between material particles in a continuum and is valid over any body without restriction on displacements (i.e. continuity, differentiability). The peridynamic equation of motion is given as follows:

$$\rho \ddot{\mathbf{u}}[\mathbf{x}, t] = \int_{\mathcal{H}} \mathbf{f}(\mathbf{u}[\mathbf{x}', t] - \mathbf{u}[\mathbf{x}, t], \mathbf{x}' - \mathbf{x}) dV_{\mathbf{x}'} + \mathbf{b}[\mathbf{x}, t] \quad (2)$$

where \mathbf{x}' is the position vector of some neighboring material location with respect to \mathbf{x} and $dV_{\mathbf{x}'}$ is the differential volume of \mathbf{x}' . \mathcal{H} describes the family of \mathbf{x}' with respect to \mathbf{x} . \mathcal{H} is typically defined by a sphere of radius δ with center \mathbf{x} . Figure 1(a) shows an illustration of a peridynamic continuum body, \mathcal{B} . It has been shown that if the analyst is only interested in the bulk response of the material, then the choice of δ is essentially arbitrary [1]. However, if the length scale is important, δ can be chosen appropriately, for example, to account for van der Waals forces in molecular dynamics modeling. It has also been proven [3] that Equation (2) reduces to the classical continuum partial differential equation in the limit as $\delta \rightarrow 0$, assuming a certain smoothness of the displacement field as required for the existence of partial derivatives.

[‡]Notation convention: Throughout this paper tensor quantities will be denoted by boldface type. First-order tensors may be referred in the text as vectors. States are denoted by uppercase bold letters with an underscore.

Equation (2) was the original formulation of the peridynamic theory, which carried a few significant shortcomings; mainly, it is an oversimplification to assume that any pair of particles interacts with each other only through a central force potential that is independent of all other local conditions. Therefore, for an isotropic, linear material there will always be an effective Poisson's ratio of $\frac{1}{4}$, similar to Navier's original elasticity theory. Another drawback of this particular model is the requirement to completely recast the constitutive behavior of a material in terms of a pairwise force function when traditionally material behavior has been formulated in terms of a stress tensor. Finally, although plasticity can be included in the bond-based theory by permitting permanent deformation of individual bonds, this results in permanent deformation of a material undergoing volumetric strain (without shear). Experimental observations of the behavior of metals have suggested that only shear deformations can involve plastic response.

With the need to address these issues, the peridynamic theory was reformulated to be more general [4]. The resulting 'state-based' peridynamic equation of motion is given in the following equation as:

$$\rho \ddot{\mathbf{u}}[\mathbf{x}, t] = \int_{\mathcal{H}} \{ \mathbf{T}[\mathbf{x}, t](\mathbf{x}' - \mathbf{x}) - \mathbf{T}[\mathbf{x}', t](\mathbf{x} - \mathbf{x}') \} dV_{\mathbf{x}'} + \mathbf{b}[\mathbf{x}, t] \quad (3)$$

where all the definitions for Equation (2) hold, and \mathbf{T} is defined as the peridynamic force–vector state. The concept of vector states is similar to that of a second-order tensor in that they both map vectors into vectors, but vector states do not have to be a linear or continuous functions. The angle brackets, $\langle \rangle$, in Equation (3) indicate the vector on which the state operates. \mathbf{T} maps a deformation–vector state into a force–vector state for each material point within \mathcal{H} . This generalization essentially allows for neighboring bonds to interact with each other and eliminates all of the shortcomings described above. Using this methodology there is a straightforward manner in which the analyst can take classical constitutive models (i.e. Hooke's law) and convert them into force–vector state descriptions [4]. Equation (3) has also been shown to reduce to Equation (1) in the limit as $\delta \rightarrow 0$, again assuming a certain smoothness of the displacement field [5].

In order to solve general problems in solid mechanics, Equation (3) is discretized and the integral is replaced with a finite sum. The resulting formula is shown as follows:

$$\rho \ddot{\mathbf{u}}[\mathbf{x}_i, t] = \sum_{j=1}^k \{ \mathbf{T}[\mathbf{x}_i, t](\mathbf{x}_j - \mathbf{x}_i) - \mathbf{T}[\mathbf{x}_j, t](\mathbf{x}_i - \mathbf{x}_j) \} V_j + \mathbf{b}[\mathbf{x}_i, t] \quad \forall i = 1, 2, \dots, \mathcal{N} \quad (4)$$

where \mathbf{x}_i represents a discrete material particle or node, and \mathbf{x}_j represents a single node within the horizon, \mathcal{H} . k represents the total number of nodes within \mathcal{H} , and \mathcal{N} represents the total number of nodes within the peridynamic body of interest. V_j is the volume of the \mathbf{x}_j node. Figure 1(b) shows an illustration of a discretized peridynamic body \mathcal{B} . Figure 1(b) is shown with a structured grid of material points; however, this is just for illustrative purposes as the grid could be completely random. This process is described in detail in Silling and Askari [6], and results in a mesh-free method of solving complex mechanics problems. An explicit time integration scheme is used to solve these equations for dynamic problems in the Sandia National Laboratories code, Emu.

Warren *et al.* [7] have recently implemented the linear elastic and elastic–plastic linear hardening models into Emu and showed convergence to analytic solutions of bending in a peridynamic bar. This paper extends this research by implementing a strain-hardening viscoplastic model into Emu,

this is the first numerical implementation of a constitutive model with this degree of complexity into the peridynamic framework. Simulations and comparisons to experimental data are included.

Because the discretized version (Equation (4)) of the peridynamic equation of motion (Equation (3)) is meshless and Lagrangian, it is worthwhile to draw a distinction between it and ‘particle methods’ such as smooth particle hydrodynamics (SPH) and element-free Galerkin [8–13]. The other methods approximate the partial differential equations of the standard theory of solid mechanics. Therefore, they inherit the difficulties of the standard theory with regard to singularities, especially the need for special treatment of cracks. In contrast, because the basic equations of the peridynamic theory are equally applicable to smooth or discontinuous deformations, no such special treatment is necessary. The discretized equation (Equation (4)) is applied everywhere, regardless of how cracks or other discontinuities evolve. One benefit of this mathematical consistency is that cracks grow without the imposition of supplemental equations that govern their nucleation, initiation, and advance. All these features emerge from the equation of motion and constitutive relation. In addition, experience with the peridynamic method has shown no tensile instability that has been reported in SPH [9].

2. PERIDYNAMIC KINEMATICS

The first step in numerically implementing a traditional (formulated in terms of stress and strain) constitutive model into the state-based peridynamic framework is finding an approximation to the local deformation gradient, \mathbf{F} , for each node. Recall from classical continuum mechanics that the deformation gradient is a local linear approximation to the true deformation defined by[§]

$$\mathbf{F} = \mathbf{I} + \mathbf{u} \nabla_{\mathbf{x}} \quad (5)$$

where \mathbf{I} is the identity tensor and $\nabla_{\mathbf{x}}$ is the gradient operator with respect to \mathbf{x} . In order for \mathbf{F} to be defined, all of the partial derivatives contained in $\mathbf{u} \nabla_{\mathbf{x}}$ must exist. This requires the displacement field to be continuously differentiable. In other forms of computational mechanics (e.g. finite element method), these partial derivatives must only be defined in a weak sense in order for \mathbf{F} to exist; we will not even make this restriction in the peridynamic formulation [14]. We will use the true deformation, defined by the deformation-vector state $\underline{\mathbf{Y}}(\xi)$ (Equation (6)), to approximate \mathbf{F}

$$\underline{\mathbf{Y}}[\mathbf{x}, t](\xi) = \xi + \boldsymbol{\eta} \quad (6)$$

where ξ is the relative position between two material points

$$\xi = \mathbf{x}' - \mathbf{x} \quad (7)$$

and $\boldsymbol{\eta}$ is the relative displacement

$$\boldsymbol{\eta} = \mathbf{u}[\mathbf{x}', t] - \mathbf{u}[\mathbf{x}, t] \quad (8)$$

$\underline{\mathbf{Y}}(\xi)$ is a vector function that associates any bond ξ with the deformed image of the bond. We now define a non-local *shape tensor* with the following integral:

$$\mathbf{K}[\mathbf{x}, t] = \int_{\mathcal{H}} \omega(|\xi|)(\xi \otimes \xi) dV_{\mathbf{x}'} \quad (9)$$

[§] $F_{ij} = \delta_{ij} + \partial u_i / \partial x_j$ using indicial notation.

where \otimes is the dyadic product operator and ω is defined as an *influence function*, which is scalar valued and dependent on $|\xi|$. In this implementation, ω is always either 0 or 1, which corresponds to whether the bond is ‘broken’ or not. Broken bonds are the method in which material failure is introduced in the peridynamic theory, and this is one of the primary advantages of the theory it is not discussed here. The reader is directed to [2, 6] for further explanations of modeling failure with peridynamics. ω could also be used as distributable influence function where certain material neighbors have more influence than others. To date, only constant influence functions have been studied with no apparent negative effects (instabilities, etc.). The integral in Equation (9) results in a positive-definite tensor when evaluated; therefore, \mathbf{K} will always be invertible. For a discrete system we can represent the non-local shape tensor for a node with the following sum:

$$\mathbf{K}[\mathbf{x}_i, t] \approx \sum_{j=1}^k \omega(|\xi|)(\xi \otimes \xi) V_j \quad (10)$$

where ξ is now

$$\xi = \mathbf{x}_j - \mathbf{x}_i \quad (11)$$

Similarly, it can be shown that the discrete \mathbf{K} in Equation (10) will be invertible as long as three non-coplanar vectors ξ are used in the formulation.

Knowing the shape tensor, the approximated deformation gradient, \mathbf{F} , at a material point \mathbf{x} is given by

$$\mathbf{F}[\mathbf{x}, t] = \left[\int_{\mathcal{H}} \omega(|\xi|)(\underline{\mathbf{Y}}(\xi) \otimes \xi) dV_{\mathbf{x}'} \right] \mathbf{K}^{-1} \quad (12)$$

Similarly, in discrete form:

$$\mathbf{F}[\mathbf{x}_i, t] \approx \left[\sum_{j=1}^k \omega(|\xi|)(\underline{\mathbf{Y}}(\xi) \otimes \xi) V_j \right] \mathbf{K}^{-1} \quad (13)$$

The deformation gradient can be shown to be exact for a constant deformation. This is always true irrespective of the location of a material point within a body, even along boundaries or near discontinuities. If we assume a constant deformation-vector state, $\underline{\mathbf{Y}}_i = F_{ip}\xi_p$, then the proof follows:

$$\begin{aligned} F_{ij} &= \left[\int_H \omega(\xi) F_{ip} \xi_p \xi_k dV_{\xi} \right] K_{kj}^{-1} \\ &= F_{ip} \left[\int_H \omega(\xi) \xi_p \xi_k dV_{\xi} \right] K_{kj}^{-1} \\ &= F_{ip} K_{pk} K_{kj}^{-1} \\ &= F_{ip} \delta_{pj} \\ &= F_{ij} \end{aligned}$$

With the deformation gradient in hand, the rest of the kinematics follows the standard definitions laid out in many texts. For completeness, the foundation used to find the *unrotated rate of deformation tensor*, \mathbf{d} will be included. First, the velocity gradient tensor is given by

$$\mathbf{L} = \dot{\mathbf{F}}\mathbf{F}^{-1} \quad (14)$$

Since \mathbf{F} is defined in material (Lagrangian) coordinates, $\dot{\mathbf{F}}$ is the material time derivative of \mathbf{F} . The velocity gradient can be decomposed into symmetric and skew-symmetric parts. The symmetric part is referred to as the rate of deformation tensor and is shown as follows:

$$\mathbf{D} = \frac{1}{2}[\mathbf{L} + \mathbf{L}^T] \quad (15)$$

If the polar decomposition theorem is applied to \mathbf{F} , we have

$$\mathbf{F} = \mathbf{V}\mathbf{R} = \mathbf{R}\mathbf{U} \quad (16)$$

where \mathbf{R} is a orthogonal tensor describing a rigid-body rotation. The tensor \mathbf{R} is calculated in the incremental formulation outlined by Taylor and Flanagan [15]. \mathbf{V} and \mathbf{U} are the left and right stretch tensors, respectively. Now we can use the right polar decomposition from Equation (16) and substitute it into Equation (14) to define the velocity gradient in another way

$$\mathbf{L} = \dot{\mathbf{R}}\mathbf{R}^T + \mathbf{R}\dot{\mathbf{U}}\mathbf{U}^{-1}\mathbf{R}^T \quad (17)$$

The term $\dot{\mathbf{R}}\mathbf{R}^T$ in Equation (17) is skew symmetric and represents a rate of rotation. The symmetric part of $\dot{\mathbf{U}}\mathbf{U}^{-1}$ is referred to as the unrotated rate of deformation tensor. Equating with Equation (15), the unrotated rate of deformation tensor can be described as shown in the following equation:

$$\mathbf{d} = \frac{1}{2}[\dot{\mathbf{U}}\mathbf{U}^{-1} + \mathbf{U}^{-1}\dot{\mathbf{U}}] = \mathbf{R}^T\mathbf{D}\mathbf{R} \quad (18)$$

3. PRINCIPAL OF MATERIAL FRAME INDIFFERENCE

The principal of material frame indifference (also referred to as objectivity) says that a constitutive law must be invariant to a change of material reference frame. Therefore, only objective quantities can be used in a constitutive equation. For this reason we chose to apply the constitutive relationship to the Cauchy stress in the unrotated configuration. The unrotated Cauchy stress, $\boldsymbol{\tau}$, is related to the rotated Cauchy stress or true stress, $\boldsymbol{\mathcal{T}}$, with the rotation tensor \mathbf{R} by the following:

$$\boldsymbol{\tau} = \mathbf{R}^T \boldsymbol{\mathcal{T}} \mathbf{R} \quad (19)$$

Because numerical techniques involve the integration of rate equations, we require that the stress rate is objective. Johnson and Bammann [16] building on the work of Green and Naghdi [17], showed if a motion is considered that differs from a given motion only by a superimposed rigid body motion, that is,

$$\mathbf{z}^* = \mathbf{a}(t) + \mathbf{M}(t)\mathbf{z} \quad (20)$$

where \mathbf{a} is a vector function of t which can be interpreted as a rigid-body translation and \mathbf{M} is a proper orthogonal tensor function of t that can be interpreted as a rotation tensor, when the motion

prescribed in Equation (20) is applied to the unrotated and rotated Cauchy stress rate tensors, the following results:

$$\dot{\boldsymbol{\tau}}^* = \dot{\boldsymbol{\tau}} \quad (21)$$

$$\dot{\mathcal{T}}^* = \dot{\mathbf{M}} \mathcal{T} \mathbf{M}^T + \mathbf{M} \dot{\mathcal{T}} \mathbf{M}^T + \mathbf{M} \mathcal{T} \dot{\mathbf{M}}^T \quad (22)$$

From Equations (21) and (22) it is clear that the unrotated Cauchy stress rate is objective, whereas the Cauchy stress rate in the rotated configuration is not. In the subsequent discussions of implementing the constitutive model, all stress quantities will be assumed to be in the unrotated configuration to ensure compliance with the principal of material frame indifference.

4. STRESS TO PERIDYNAMIC STATE CONVERSION

If we assume that the unrotated Cauchy stress tensor is a known quantity, we can rotate back into the deformed configuration using the rotation tensor from the polar decomposition

$$\mathcal{T} = \mathbf{R} \boldsymbol{\tau} \mathbf{R}^T \quad (23)$$

We can now convert the rotated Cauchy stress tensor into the first Piola–Kirchhoff stress tensor, $\boldsymbol{\sigma}$, with the relationship

$$\boldsymbol{\sigma} = \det(\mathbf{F}) \mathcal{T} \mathbf{F}^{-T} \quad (24)$$

and the first Piola–Kirchhoff stress tensor can be converted into the force–vector state with the following relationship [4]:

$$\underline{\mathbf{T}}(\xi) = \omega(|\xi|) \boldsymbol{\sigma} \mathbf{K}^{-1} \xi \quad (25)$$

The force–vector state, $\underline{\mathbf{T}}(\xi)$, can then be substituted back into Equation (4) and numerically integrated to find the displacements at the next time step. Then the process is repeated for the desired number of time steps to get a final solution. This method is purely meshless Lagrangian in that it produces all spatial information (displacement, velocity, acceleration, stress, strain) at each node for each time step without the need for Gauss integration points and interpolation of nodal values.

5. VON MISES PLASTICITY

Data used to determine constitutive model parameters are usually collected during a uniaxial tension test. We need a way to use this information to model arbitrary deformations. This theory is well developed in many texts [18, 19] and is commonly referred to as von Mises plasticity theory. It has been observed experimentally that, as a first approximation, metals yield as a result of shear deformations (independent of hydrostatic pressure). If this assumption of pressure independence is valid, it follows that yielding depends only on the deviatoric stress, which is defined in the following equation:

$$\mathbf{S} = \boldsymbol{\tau} - \frac{1}{3} \text{tr}(\boldsymbol{\tau}) \mathbf{I} \quad (26)$$

where τ is the unrotated Cauchy stress tensor and $\text{tr}(\tau) = \tau_{11} + \tau_{22} + \tau_{33}$. The second term in Equation (26) represents the hydrostatic pressure, and by subtracting it from the Cauchy stress only the stress as a result of shear deformation is left. If we assume that the state of stress as measured during a uniaxial tension test at the onset of yielding is defined by a stress, G , then it follows that:

$$\tau = \begin{bmatrix} G & 0 & 0 \\ 0 & 0 & 0 \\ 0 & 0 & 0 \end{bmatrix} \quad (27)$$

the deviatoric stress tensor corresponding to this state of stress

$$\mathbf{S} = \begin{bmatrix} \frac{2}{3}G & 0 & 0 \\ 0 & -\frac{1}{3}G & 0 \\ 0 & 0 & -\frac{1}{3}G \end{bmatrix} \quad (28)$$

and the magnitude[‡] of the deviatoric stress tensor is defined as

$$S = |\mathbf{S}| = \sqrt{\frac{2}{3}}G \quad (29)$$

The term $\sqrt{\frac{2}{3}}G$ represents the extent of the yield surface in stress space. Stress space is a three-dimensional space where the axes represent the principal stresses. In von Mises plasticity theory the yield surface is always a cylinder with the central axis along the line $\sigma_I = \sigma_{II} = \sigma_{III}$, where σ_I , σ_{II} , and σ_{III} are the principal stresses. A state of stress can never be outside the yield surface, but can sit on the yield surface indefinitely, and the yield surface can change in size, depending on G .

Once the value of the deviatoric stress magnitude has exceeded G the material is said to be yielded and deforms according to the *flow rule*, which describes the plastic deformation. To begin the discussion of the flow rule we will define the total deviatoric strain rate to be as follows:

$$\dot{\mathbf{e}} = \mathbf{d} - \frac{1}{3}\text{tr}(\mathbf{d})\mathbf{I} \quad (30)$$

We will assume that the total deviatoric strain rate can be additively decomposed into purely elastic and plastic parts as shown as follows:

$$\dot{\mathbf{e}} = \dot{\mathbf{e}}^e + \dot{\mathbf{e}}^p \quad (31)$$

This implies that the elastic part, $\dot{\mathbf{e}}^e$, is fully recoverable and the plastic part, $\dot{\mathbf{e}}^p$, results in permanent strain. The elastic part of the deviatoric strain rate tensor can then be written according to Hooke's law for stress and strain rates as follows:

$$\dot{\mathbf{e}}^e = \frac{\dot{\mathbf{S}}}{2\mu} \quad (32)$$

[‡]The magnitude of a tensor \mathbf{A} is defined by $|\mathbf{A}| = \sqrt{A_{ij}A_{ij}}$ using Einstein indicial summation.

where μ is the shear modulus. In order to define the plastic part of the deviatoric strain rate tensor we will assume a flow rule of the form

$$\dot{\mathbf{e}}^p = \dot{\lambda} \mathbf{Q} \quad (33)$$

where $\dot{\lambda}$ is a yet undetermined scalar and \mathbf{Q} is a unit tensor in the direction of deviatoric stress defined as follows:

$$\mathbf{Q} = \frac{\mathbf{S}}{S} \quad (34)$$

Equation (33) is called an *associated* flow rule because the direction of plastic flow is associated with the direction of deviatoric stress. This is one of the most common flow rules and is almost always used to model plasticity in metals that deform with pressure invariance.

6. YIELD SURFACE DETERMINATION

At each time step and for each peridynamic node, we must calculate the scalar value representing the extent of the yield surface. If we assume a yielded stress magnitude, G , that is defined as a function of *equivalent plastic strain* and its time derivative *equivalent plastic strain rate* (ε^p and $\dot{\varepsilon}^p$, respectively), or in notational form

$$G = f(\varepsilon^p, \dot{\varepsilon}^p) \quad (35)$$

then in order to define G at a time, t , we must decide which values of ε^p and $\dot{\varepsilon}^p$ to use. The most straightforward method is to use a backward explicit scheme that defines G as

$$G_t = f\left(\varepsilon_{t-\Delta t}^p, \frac{\varepsilon_{t-\Delta t}^p - \varepsilon_{t-2\Delta t}^p}{\Delta t}\right) \quad (36)$$

where Δt is a constant time-step increment. The constant time-step assumption is used here to keep the notation tractable, but in general is not a requirement. While this is a straightforward method for defining G_t , stability calculations performed by Silling [20] have shown this method to be unstable for all but trivial cases. A different approach was determined by the same stability calculations to be stable without additional restriction on time-step size beyond that for traditional explicit finite differencing methods. This approach is adopted here and is a backward implicit definition of the form:

$$G_t = f\left(\varepsilon_{t-\Delta t}^p, \frac{\varepsilon_t^p - \varepsilon_{t-\Delta t}^p}{\Delta t}\right) \quad (37)$$

Here, G_t is implicit in ε_t^p and therefore not a straightforward calculation. The following steps describe how we will solve for G_t by casting the problem in a framework involving only scalars for simplicity. First, we will define the equivalent plastic strain rate, $\dot{\varepsilon}^p$, to be

$$\dot{\varepsilon}^p = \sqrt{\frac{2}{3}} |\dot{\mathbf{e}}^p| \quad (38)$$

The $\sqrt{\frac{2}{3}}$ term appears by convention similar to that which results in Equation (29) because $\dot{\varepsilon}^p$ is the plastic strain rate that would be measured in a uniaxial tension test. If we substitute Equation (33) into Equation (38), remembering that \mathbf{Q} is a unit tensor we have the following:

$$\dot{\varepsilon}^p = \sqrt{\frac{2}{3}} \dot{\lambda} \quad (39)$$

Now we define a scalar, \dot{e} , which is the projection of the total deviatoric strain rate tensor in the direction of deviatoric stress, we have

$$\dot{e} = \dot{\varepsilon} : \mathbf{Q} \quad (40)$$

where: is the tensor dot product operator. Now we apply a similar relationship to $\dot{\varepsilon}^e$

$$\dot{e}^e = \dot{\varepsilon}^e : \mathbf{Q} \quad (41)$$

If we combine Equations (33), (40), and Equation (41) with Equation (31), we have the relationship that follows:

$$\dot{e} = \dot{e}^e + \dot{\lambda} \quad (42)$$

Substituting Equation (32) into Equation (41), we find that the magnitude of elastic deviatoric strain rate can be described as shown as follows:

$$\dot{e}^e = \frac{\dot{S}}{2\mu} \quad (43)$$

Next we substitute Equation (43) into Equation (42) and multiply the result by Δt in order to convert the rate terms into increments, which results in the following:

$$\Delta e = \frac{\Delta S}{2\mu} + \Delta \lambda \quad (44)$$

If we assume that Δt represents a time increment between times t and $t - \Delta t$, we can expand the deviatoric strain increment and slightly rearrange Equation (44) to provide

$$\Delta e_{t-\Delta t/2} - \frac{S_t - S_{t-\Delta t}}{2\mu} - \Delta \lambda_{t-\Delta t/2} = 0 \quad (45)$$

Assuming that the material is yielded at the time t , we can substitute Equation (29) into Equation (45) to have:

$$\Delta e_{t-\Delta t/2} - \frac{\sqrt{\frac{2}{3}} G_t - S_{t-\Delta t}}{2\mu} - \Delta \lambda_{t-\Delta t/2} = 0 \quad (46)$$

If we multiply Equation (39) by Δt to once again convert rates into increment values, we can substitute the result into Equation (37) to redefine our yield function as follows:

$$G_t = f \left(\varepsilon_{t-\Delta t}^p, \sqrt{\frac{2}{3}} \frac{\Delta \lambda_{t-\Delta t/2}}{\Delta t} \right) \quad (47)$$

Finally, we substitute Equation (47) into Equation (46) to get

$$\Delta e_{t-\Delta t/2} - \Delta \lambda_{t-\Delta t/2} - \frac{1}{2\mu} \left[\sqrt{\frac{2}{3}} f \left(\varepsilon_{t-\Delta t}^p, \sqrt{\frac{2}{3}} \frac{\Delta \lambda_{t-\Delta t/2}}{\Delta t} \right) - S_{t-\Delta t} \right] = 0 \quad (48)$$

Equation (48) involves only terms that are defined at time step t , except for $\Delta \lambda$, which can be solved with a numerical root solver. If the left-hand side of Equation (48) is continuous, it can be differentiated with respect to $\Delta \lambda$; therefore, a Newton–Raphson method can be used if desired. However, the left-hand side of Equation (48) is a monotonically decreasing function of $\Delta \lambda$, and as $\Delta \lambda \rightarrow 0$, the slope of this function becomes infinity and Newton’s method will not converge. Therefore, for the simulations that will be shown in subsequent sections, a bisection method was used to solve for $\Delta \lambda$. The root was assumed to be $0 < \Delta \lambda < 1$ and has converged in all test cases. Generally, $\Delta \lambda$ is a very small positive number much less than 1. Perhaps a numerical root solver such as Brent’s method would be the most efficient algorithm to use because it guarantees convergence if the root is bounded and also converges faster than the bisection method alone.

Once $\Delta \lambda$ is known, G_t can be found by substituting $\Delta \lambda$ into the relationship shown in Equation (47).

7. EVALUATION OF STRESS TENSOR

Once G_t is known, we can decide whether a node is yielded or not by comparing the magnitude of the deviatoric stress with the scalar value indicating the extent of the yield surface. First, we assume a ‘trial’ deviatoric stress by considering only an elastic deformation increment across a time step as follows:

$$\mathbf{S}_t^{\text{tr}} = \mathbf{S}_{t-\Delta t} + 2\mu \Delta \mathbf{e}_{t-\Delta t/2} \quad (49)$$

Now we can define the deviatoric stress at a time step, t , according to the following:

$$\mathbf{S}_t = \begin{cases} \mathbf{S}_t^{\text{tr}}, & |\mathbf{S}_t^{\text{tr}}| < \sqrt{\frac{2}{3}} G_t \\ \sqrt{\frac{2}{3}} G_t \mathbf{Q}_t^{\text{tr}}, & |\mathbf{S}_t^{\text{tr}}| \geq \sqrt{\frac{2}{3}} G_t \end{cases} \quad (50)$$

Geometrically, the second part of Equation (50) represents a ‘radial return to the yield surface,’ which ensures that any stress state lies within or on the yield surface for all time. With the new deviatoric stress tensor we can easily find the new value of Cauchy stress as shown in the following equation:

$$\boldsymbol{\tau}_t = \mathbf{S}_t + p_t \mathbf{I} \quad (51)$$

where p_t is the hydrostatic pressure defined as

$$p_t = p_{t-\Delta t} + \mathcal{K} \text{tr}(\mathbf{d}_{t-\Delta t/2}) \Delta t \quad (52)$$

and \mathcal{K} is the materials bulk modulus.

8. EVALUATION OF EQUIVALENT PLASTIC STRAIN

Once a stress tensor is known in time t , the only remaining operation in this time step is to find the updated value of equivalent plastic strain. The most straightforward method of evaluating equivalent plastic strain would be to simply substitute the value of $\Delta\lambda$ into the differenced form of Equation (39) and solve for the equivalent plastic strain at time t . A more general form will be used because, in cases where G_t is not dependent on $\dot{\varepsilon}^p$, the value of $\Delta\lambda$ does not have a physical meaning. However, the equivalent plastic strain can change over a time step through mechanisms other than rate dependence. If we assume that a scalar value of deviatoric plastic strain is defined in a similar fashion to the elastic and total deviatoric strains defined earlier, we have:

$$\dot{\varepsilon}^p = |\dot{\mathbf{e}}^p| = \dot{\mathbf{e}}^p : \mathbf{Q} \quad (53)$$

If we solve Equation (31) for $\dot{\mathbf{e}}^p$ and substitute into Equation (53), we have

$$\dot{\varepsilon}^p = (\dot{\mathbf{e}} - \dot{\mathbf{e}}^e) : \mathbf{Q} \quad (54)$$

then we substitute Equation (43) into Equation (54) to yield the following:

$$\dot{\varepsilon}^p = \left(\dot{\mathbf{e}} - \frac{\dot{\mathbf{S}}}{2\mu} \right) : \mathbf{Q} \quad (55)$$

Finally, we will take Equation (55) and substitute it into Equation (39), take the differenced form by multiplying through by Δt , and solve for ε_t^p to give the following result:

$$\varepsilon_t^p = \varepsilon_{t-\Delta t}^p + \sqrt{\frac{2}{3}} \left(\Delta \mathbf{e}_{t-\Delta t/2} - \frac{\mathbf{S}_t - \mathbf{S}_{t-\Delta t}}{2\mu} \right) : \mathbf{Q}_{t-\Delta t/2} \quad (56)$$

where

$$\mathbf{Q}_{t-\Delta t/2} = \frac{\mathbf{Q}_t + \mathbf{Q}_{t-\Delta t}}{2} \quad (57)$$

9. CONSTITUTIVE MODEL

With the fundamental theory in hand, we will turn to the numerical implementation of the constitutive model. The viscoplastic constitutive law we implemented was used in Camacho and Ortiz [21] and modified by Warren and Tabbara [22] to ignore temperature effects resulting in the form shown as follows:

$$G = g \left(1 + \frac{\dot{\varepsilon}^p}{\dot{\varepsilon}_0^p} \right)^{1/m} \quad (58)$$

where $\dot{\varepsilon}^p$ is the equivalent plastic strain rate, $\dot{\varepsilon}_0^p$ is a reference equivalent plastic strain rate, m is the strain-rate exponent, and g defines the dynamic yield stress and is given by the following equation:

$$g = Y \left(1 + \frac{\varepsilon^p}{\varepsilon_0^p} \right)^{1/n} \quad (59)$$

where Y is the quasi-static yield stress, ε^p is the equivalent plastic strain, ε_0^p is the reference equivalent plastic strain, and n is a strain hardening parameter. This model is a phenomenological model with n , m , ε_0^p , and $\dot{\varepsilon}_0^p$ being curve fit parameters determined from the experimental data.

Momentarily returning to Equation (48), we show the relationship that we will use to numerically find $\Delta\lambda$. If we use the constitutive model of Equation (58) as the yield function, Equation (48) becomes

$$\Delta e_{t-\Delta t/2} - \Delta \lambda_{t-\Delta t/2} - \frac{1}{2\mu} \left[\sqrt{\frac{2}{3}} Y \left(1 + \frac{\varepsilon_{t-\Delta t}^p}{\varepsilon_0^p} \right)^{1/n} \left(1 + \sqrt{\frac{2}{3}} \frac{\Delta \lambda_{t-\Delta t/2}}{\Delta t \dot{\varepsilon}_0^p} \right)^{1/m} - S_{t-\Delta t} \right] = 0 \quad (60)$$

And it follows that the yield surface G_t will be:

$$G_t = Y \left(1 + \frac{\varepsilon_{t-\Delta t}^p}{\varepsilon_0^p} \right)^{1/n} \left(1 + \sqrt{\frac{2}{3}} \frac{\Delta \lambda_{t-\Delta t/2}}{\Delta t \dot{\varepsilon}_0^p} \right)^{1/m} \quad (61)$$

10. NUMERICAL SIMULATIONS

The viscoplastic constitutive model presented in the previous sections was implemented into the explicit dynamics code Emu. In a typical finite element code, when a new model is introduced it is customary to run a uniaxial stress test on a single element in order to verify that the constitutive response reproduces the experimental data. In the peridynamic framework, a single node simulation will not suffice because a minimum number of nodes is necessary to calculate a stress tensor. Instead, a model consisting of 3825 nodes representing a cylindrical tensile test specimen was simulated for comparison with experimental data. The simulation was run at an engineering strain rate of 8300 s. Boundary conditions are applied by giving a region of nodes on either ends of the bar a constant velocity. This could also be achieved by applying a prescribed displacement or body force density to a region of nodes. The material parameters used correspond to a data fit to 6061-T6 aluminum provided in Song *et al.* [23]. The experiments were conducted using a pulse-shaped Kolsky bar experiments to ensure a constant engineering strain rate of 8300 s. The constitutive parameters are as follows: $E = 68.9$ GPa, $\nu = 0.333$, $Y = 276$ MPa, $n = 13.5$, $m = 44.0$, $\varepsilon_0^p = 0.001$ s, and $\dot{\varepsilon}_0^p = 1000$ s. Figure 2 shows true stress as a function of Lagrangian strain for the simulations. The strain measurement from the simulation was calculated by using the Green-St. Venant formulation from the approximate deformation gradient as shown in the following:

$$\mathbf{E} = \frac{1}{2} (\mathbf{F}^T \mathbf{F} - \mathbf{I}) \quad (62)$$

The numerical implementation of the constitutive model matches the experimental data very well. Currently, the constitutive model is only implemented in an explicit dynamics code, which makes running the simulation at quasi-static rates nearly impossible due to conditions that require a very small time step; therefore, only a comparison at the high rate was done.

In order to further validate the numerical implementation of the constitutive model into Emu, Taylor impact experimental results were simulated. A set of Taylor impact tests were conducted on 6061-T6 aluminum by Anderson *et al.* [24]. This data included normalized length and diameter

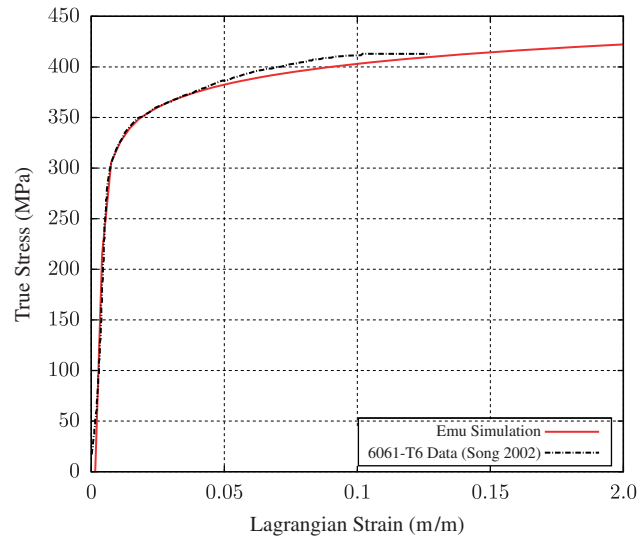


Figure 2. Comparison of experimental data with numerical simulation at nominal engineering strain rate of 8300 s.⁻¹

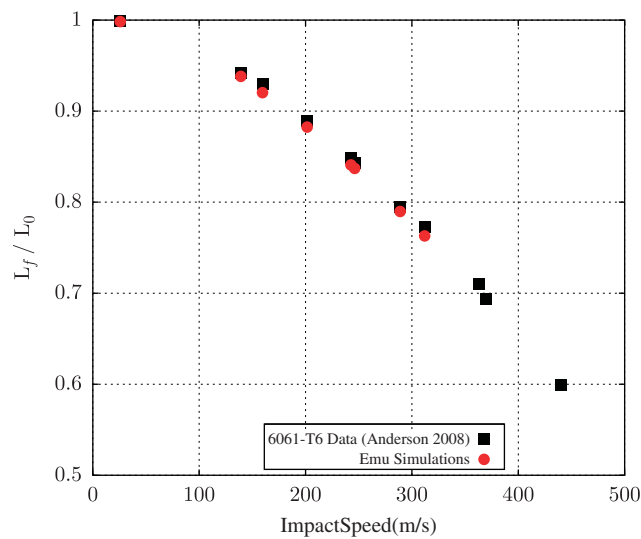


Figure 3. Normalized length comparison.

measurements as well as a selection of dynamic structured light (DSL) images of the deformed specimens. The test specimens were 3.175 cm long with a diameter of 6.35 mm ($L/D=5$). The tests were conducted at impact speeds between 26 and 440 m/s; however, at an impact speed of 363 m/s and above, post test examination of the Taylor impact specimens showed significant ‘mushrooming’ and failure at the impact end. While failure can be modeled with peridynamics, it is beyond the scope of this paper; therefore, these experiments were not attempted in numerical

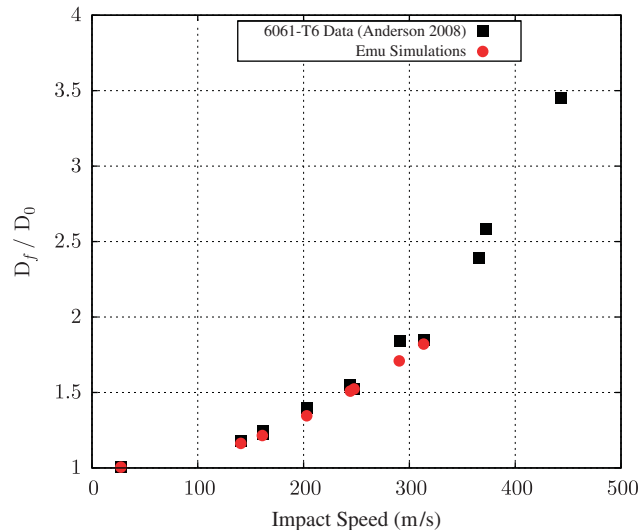


Figure 4. Normalized diameter comparison.

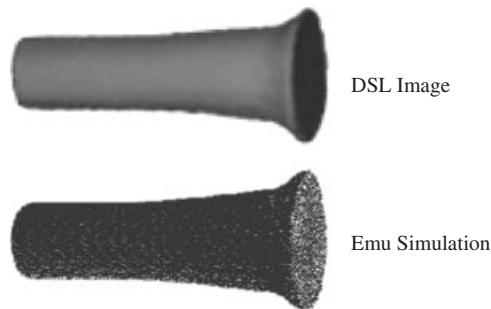


Figure 5. Qualitative comparison of post test deformation from DSL image with numerical simulation at 289m/s impact speed.

simulation. The Emu simulations were performed with a resolution of 40 nodes across the diameter of the specimen, resulting in 252 800 total nodes. The length scale parameter, δ , was chosen to be $3.05 \cdot \Delta x$, where Δx is the distance between the material particles. Simulations were also run at $\delta = 4 \cdot \Delta x$ and $\delta = 5 \cdot \Delta x$ to investigate the length scale effect. As expected because these simulations were intended to investigate bulk response (change in length/diameter), the change in δ had little to no effect on the simulation results. Figure 3 shows the normalized length (final length divided by initial length) for the Taylor impact experiments and the numerical simulations using the Emu code. Figure 4 shows the normalized diameter at the impact face for the Taylor experiments and the numerical simulations. Both the length and the diameter calculations match the experimental data well. For a qualitative comparison of deformation, one of the Emu simulations is shown next to the DSL image from tests conducted at 289m/s impact speed in Figure 5. Here again we see a good qualitative comparison of the deformation.

These simulations suggest the viability of using peridynamics to model materials that exhibit viscoplasticity with hardening.

11. CONCLUSION

In this paper, an elastic viscoplastic constitutive relationship is implemented into a peridynamic numerical analysis code with the use of force–vector states. The model is phenomenological and uses parameters curve fit to the experimental data. The model was fit to high strain-rate constitutive data taken from Kolsky bar experiments on 6061-T6 aluminum. The model is then used to reproduce the experimental results from Taylor impact tests of aluminum. The normalized length and diameter results from the calculations match the experimental results very well, and qualitative comparisons of post test deformation also compare well. This paper demonstrates the ability to utilize conventional constitutive models within the state-based peridynamic framework.

Future work in this area will include utilizing these viscoplastic constitutive models within peridynamic computational mechanics codes to predict material response during failure. Material failure will be handled through an energy criterion to determine when two material particles no longer interact with each other through the force–vector states. This will allow straightforward modeling of crack propagation within structures and hopefully provide a method for the modeling of penetration, perforation, and other impact events.

ACKNOWLEDGEMENTS

Sandia is a multiprogram laboratory operated by Sandia Corporation for the United States Department of Energy under Contract DE-AC04-94AL85000. This work was supported by the DOE/DoD Joint Munitions Technology Program. The first author would like to personally thank Dr Paul Taylor for valuable discussions involving the theory of plasticity in solid mechanics.

REFERENCES

1. Silling SA. Reformulation of elasticity theory for discontinuities and long-range forces. *Journal of the Mechanics and Physics of Solids* 2000; **48**(1):175–209.
2. Silling SA. Dynamic fracture modeling with a meshfree peridynamic code. In *Computational Fluid and Solid Mechanics*, Bathe KJ (ed.). Elsevier: Amsterdam, 2003; 641–644.
3. Silling SA, Zimmermann M, Abeyaratne R. Deformation of a peridynamic bar. *Journal of Elasticity* 2003; **73**(1):173–190.
4. Silling SA, Epton M, Weckner O, Xu J, Askari E. Peridynamic states and constitutive modeling. *Journal of Elasticity* 2007; **88**:151–184.
5. Silling SA, Lehoucq RB. Convergence of peridynamics to classical elasticity theory. *Journal of Elasticity* 2008; **93**:13–37.
6. Silling SA, Askari E. A meshfree method based on the peridynamic model of solid mechanics. *Computers and Structures* 2005; **83**(17–18):1526–1535.
7. Warren TL, Silling SA, Askari E, Weckner O, Epton MA, Xu J. A non-ordinary state-based peridynamic method to model solid material deformation and fracture. *International Journal of Solids and Structures* 2009; **46**(5):1186–1195.
8. Monaghan J. An introduction to SPH. *Particle Methods in Fluid Dynamics and Plasma Physics*, Proceedings from the Workshop held on 13–15 April 1987, Los Alamos, U.S.A., 1987; 89.
9. Li S, Liu WK. Meshfree and particle methods and their applications. *Applied Mechanics Review* 2002; **55**:1–34.
10. Gao H, Klein P. Numerical simulation of crack growth in an isotropic solid with randomized internal cohesive bonds. *Journal of the Mechanics and Physics of Solids* 1998; **46**(2):187–218.

11. Delaplace A, Ibrahimbegovic A. Performance of time-stepping schemes for discrete models in fracture dynamic analysis. *International Journal for Numerical Methods in Engineering* 2006; **65**(9):1527–1544.
12. Hoover W, Hoover C, Kum O, Castillo V, Posch H, Hess S. *Smooth Particle Applied Mechanics*. World Scientific: Singapore, 2006.
13. Rabczuk T, Belytschko T, Xiao S. Stable particle methods based on Lagrangian kernels. *Computer Methods in Applied Mechanics and Engineering* 2004; **193**(12–14):1035–1063.
14. Askari E, Bobaru F, Lehoucq RB, Parks ML, Silling SA, Weckner O. Peridynamics for multiscale materials modeling. *Journal of Physics: Conference Series* 2008; **125**:012078.
15. Flanagan DP, Taylor LM. An accurate numerical algorithm for stress integration with finite rotations. *Computer Methods in Applied Mechanics and Engineering* 1987; **62**(3):305–320.
16. Johnson G, Bammann D. A discussion of stress rates in finite deformation problems. *International Journal of Solids and Structures* 1983; **20**(8):725–737.
17. Green AE, Naghdi PM. A note on invariance under superposed rigid body motions. *Journal of Elasticity* 1977; **9**(1):1–8.
18. Hill R. *The Mathematical Theory of Plasticity*. Oxford University Press: Oxford, 1998.
19. Malvern LE. *Introduction to the Mechanics of a Continuous Medium*. Prentice-Hall: Englewood Cliffs, NJ, 1969.
20. Silling SA. Stability and accuracy of differencing schemes for viscoplastic model in wavecodes. *SAND Report SAND91-0141*, Sandia National Laboratories, 1991.
21. Camacho GT, Ortiz M. Adaptive Lagrangian modelling of ballistic penetration of metallic targets. *Computer Methods in Applied Mechanics and Engineering* 1997; **142**(3–4):269–301.
22. Warren TL, Tabbara MR. Simulations of the penetration of 6061-T6511 aluminum targets by spherical-nosed VAR 4340 steel projectiles. *International Journal of Solids and Structures* 2000; **37**(32):4419–4435.
23. Song B, Chen WW, Frew DJ. Split-Hopkinson bar testing of an aluminum with pulse shaping. *Proceedings of the JSME/ASME International Conference on Materials and Processing*. ASME: Honolulu, HI, 2002.
24. Anderson Jr C, Nicholls A, Chocron I, Ryckman R. Taylor anvil impact. *AIP Conference Proceedings*, vol. 845. AIP: New York, 2006.